

A synthetic inflow generation method using the attached eddy hypothesis

Pramod Subbareddy*, David Peterson* Graham V. Candler[†] & Ivan Marusic[‡]

University of Minnesota, Minneapolis, MN 55455

The attached eddy hypothesis is used to develop a means of generating synthetic turbulent boundary layers. Fluctuating velocity fields are created from simple vortex shapes using the Biot-Savart law. These are superposed with mean velocity profiles from experiment or RANS to create boxes of data which can be fed in through the inflow plane of a simulation. This provides realistic time varying inflow data. The method is computationally inexpensive compared with other synthetic inflow generation methods. Two flows are investigated using this approach. In the first, detached eddy simulation is used to compute normal and angled injection of helium into supersonic turbulent crossflows at Mach numbers 3 and 4 respectively. The diameter of the injector in each case is comparable to the boundary layer thickness of the crossflow and it is to be expected that fluctuations in the turbulent boundary layer play an important role in the dynamics of the jet. A comparison of the helium mass fraction in the flow field is made with experimental data and the results are encouraging. The second case considered is a supersonic turbulent mixing layer with a convective Mach number of 0.46 and a Reynolds number of $12 \times 10^6/m$ (based on the velocity difference and average ρ and μ). The two streams are brought together across a thin splitter plate and the boundary layers on both sides are turbulent. Simulations are performed with steady inflow conditions and with the synthetic turbulent flow fields. The DES methodology is used for subgrid modelling and results are compared with the experiments of Goebel and Dutton. With unsteady inflow, the comparison with experiment was found to be very good.

Introduction

Advances in technology and numerical methods have, in recent years, facilitated the employment of Direct Simulations, Large Eddy Simulations and a host of hybrid RANS/LES methodologies. All these methods set out to resolve a significant range of energy containing length and time scales. Many of the target flowfields for these computations involve an inflow boundary at which space and time-varying velocity fields need to be imposed. If the region around the inflow boundary is steady, one could impose a stationary boundary condition. In practice, however, inflow boundaries are frequently placed in turbulent regions of the flow. In the absence of symmetries such as in periodic flows, the specification of the inflow velocity is substantially more difficult and plays a crucial role in the development of the flow downstream of the inlet.

The velocity specified at these boundaries must reflect the space and time scales the numerical method intends to resolve. If the inflow consists of an incoming boundary layer, the range of structures that are known to be present (horseshoe vortices, streamwise vortices etc.) must be represented, ideally with the correct

*Graduate Research Assistant. AIAA Student Member.

[†]Professor. AIAA Associate Fellow.

[‡]AIAA Member. Professor. Department of Aerospace Engineering and Mechanics, 107 Akerman Hall, 110 Union Street SE, Minneapolis, MN 55455.

spectrum, RMS values and phase information. For example, in computations of mixing layers, computing the developing boundary layers on the splitter plate would use a significant fraction of the available computing resources. Instead, boundary layer profiles computed using cheaper means (such as RANS, experimental profiles) could be (and frequently are) specified at the trailing edge of the splitter plate and augmented with perturbations of the flow variables. A brief but comprehensive survey of current inflow generation methods can be found in the paper by Keating *et al.*¹

In this paper, we propose a means of generating realistic turbulent flow fields (specifically for turbulent boundary layers) using the attached eddy hypothesis. In section I, we provide a sketch of the underlying theory and the method by which we propose to generate the synthetic flows. Section II talks about *a priori* tests on data thus generated. The numerical method is presented in section III and section IV presents results from using these inflow fields on a few test cases.

I. Attached Eddy Hypothesis

Perry and Chong⁴ and Perry, Henbest and Chong⁵ used the hairpin vortex shape as a representative unit in a kinematic model for wall turbulence. The model relies on Townsend's^{2,3} attached eddy hypothesis and is based on an assemblage of eddies with a range of length scales with varying population densities per eddy length scale. The term 'attached' derives from the fact that the characteristic length scale is in proportion to the distance the eddy extends from the wall. Later work by Perry and Marusic⁶ and Marusic and Perry⁷ extended the basic model to compute second-order statistics, including spectra and showed good quantitative agreement for values of the Reynolds stress tensor given an experimentally measured mean velocity field for a range of wall bounded flows. Figure (1) shows an idealized sketch of a typical attached hairpin eddy that is considered in the above ensembles. The parameters involved are the size of the eddy, δ_e , (not to be confused with boundary layer thickness), the circulation, κ (assumed to be constant for a given flow), the core diameter, r_0 (which scales with δ_e), and the inclination of the structure to the mean flow. The vorticity magnitude is assumed to have a gaussian distribution about the centerline of the structure in a plane perpendicular to the direction of the vorticity at any given point.

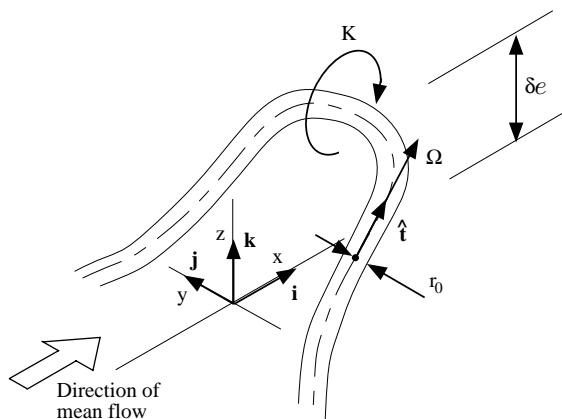


Figure 1. Sketch of a typical hairpin eddy

The work in the papers mentioned above considers a random distribution of eddies in the plane of the wall. Recent studies suggest that the above assumption is not strictly accurate, in the sense that hairpin vortices are found to be spatially aligned, forming correlated 'packets' or trains organized along the streamwise direction. The evidence for spatial coherence has come from both experimental⁸⁻¹⁰ and numerical¹¹⁻¹³ studies. Marusic¹⁴ extended the attached eddy model of Perry and Marusic⁶ to include coherent packets of vortices and found that these aggregates are statistically significant for Reynolds stresses and transport

processes in the logarithmic region of wall bounded flow. Given a candidate eddy shape one could distribute them in the plane of the wall, either randomly or in the form of packets/trains. The fluctuating velocity field due to these eddies (and their images in the wall) is easily calculated using the Biot-Savart law (note that this field is divergence free) and superimposed on a mean velocity profile obtained either from experiment or a RANS calculation. It must be pointed out that the velocity field due to the eddies does not have a zero mean. The mean contribution due to the eddies is subtracted off the flow field before the velocity profiles from RANS/experiment are imposed. Thus only the fluctuating component of the field is used. The no-slip condition at the wall needs to be separately enforced. We do this using van Driest type damping functions. Details are provided in the sections to follow.

Synthetic inflow fields using the attached eddy hypothesis

The inflow boundaries we consider are restricted to those having an incoming turbulent boundary layer. This is a small, but important, subset of inlet boundary conditions.

The idea is relatively simple. Consider a domain which extends a small distance (of the order of a few boundary layer thicknesses) upstream of the inflow boundary. We run a separate, ‘precursor’ calculation on this domain using an inexpensive RANS method. This establishes the mean velocity profiles (and thermodynamic profiles for compressible flow) at the inflow plane (which is set to be the exit plane of the precursor grid) and upstream of it. In many cases, these profiles can be verified or supplemented by existing experimental data.

The next step is to distribute a collection of eddies in the plane of the wall and use the Biot-Savart law to compute the associated velocity field. A variety of distributions could be used. Depending on the level of sophistication required, one could use a random distribution or arrange them in trains to correspond with the notion of ‘packets’. The restriction is that the fluctuating velocity field should reproduce the correct statistics (RMS values, spectra and Reynolds stresses) to a certain tolerance. This establishes a box of data which can be fed in a time-dependent manner through the inflow plane. One could choose the box size such that the ends are uncorrelated, which would enable us to use the data in a time-periodic manner. Increasing the size of the box does not place undue demands on the computation, since the precursor ‘box’ is set up prior to the actual simulation.

The paper by Marusic and Perry⁷ considered several shapes for the vortex structures in their model. Essentially, these are simplified vortex skeletons consisting of straight line segments. This simplifies the process of evaluating the Biot-Savart integral considerably. Figure (2) shows two such configurations. The structure in figure (2a) consists of a simple \square shaped eddy with two ‘legs’ inclined to the streamwise direction and a bridge connecting them, along the span. In figure (2b), the legs are joined to line segments (‘tails’), which are at a shallower inclination to the wall and are meant to mimic the quasi-streamwise vortices which populate the buffer and inner regions of a boundary layer. Needless to say, these are just two out of several possible models and many refinements are possible. In this paper, we use the simpler \square shaped structure shown in figure (2a). A hierarchy of scales is generated by geometrically scaling one such parent eddy by predetermined scaling factors (factors of two are used in this paper).

A procedure to construct the velocity field is given below. For simplicity, we assume that the flow corresponds to a flat plate turbulent boundary layer. The flow direction is assumed to be along x and the wall normal direction is z . The inflow boundary is assumed fixed at a given x location.

- Determine the mean velocity and thermodynamic profiles at the inflow location. The time step to be used in the actual DES simulation, Δt , is used to determine the streamwise spacing in the precursor grid using $\Delta x = 0.8U_\infty \Delta t$. (A mean convection velocity of $0.8U_\infty$ for the structures is assumed)
- Compute the friction velocity u_τ and the boundary layer thickness δ . The kinematic viscosity ν is assumed to be known or is determined, using for e.g., Sutherland’s law.
- Construct the precursor box grid using Δx determined as above and the grid at the inflow plane of the simulation.

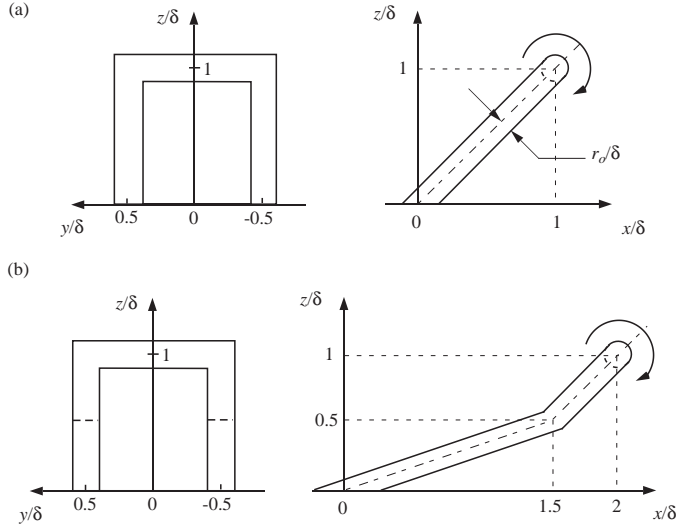


Figure 2. Typical skeleton hairpin eddies consisting of straight line segments used in the calculations. x is the streamwise direction, y is spanwise and z is the wall normal direction. δ denotes the size of the eddy in a particular hierarchy.

- The population density, p , (number of eddies in a square box of dimensions $\delta \times \delta$) of the largest scale eddies (of size δ) is assumed. We use the value $p = 1/2$. The population density for the following hierarchies are $2p$, $4p$ etc. It follows that an inverse power law for the probability density function of the eddy scales is implicitly assumed. This is consistent with the ideas of Townsend^{2,3} and others.⁴⁻⁷ The circulation (the measure of the net vorticity assumed to ‘belong’ to an eddy) also needs to be estimated. We assume a value $\kappa = Cu_\tau\delta$, where $C = 0.025$. The assumption being made here is that a fraction of the viscous sublayer, which has a velocity scale u_τ , rolls up to form these structures.
- The eddies are distributed in the x - y plane in a random fashion.
- The Biot-Savart law is used to compute the (solenoidal) velocity field due to the randomly distributed eddies (and their images in the wall) at each grid point. The non-zero mean field due to the eddies alone is subtracted and the mean velocity profile (RANS/experiment) is added on. Note that the use of simple vortex skeletons consisting of straight line segments considerably simplifies this step, since simple analytical expressions can be derived for the velocity induced at a point due to a straight line vortex segment of known net circulation and distribution of vorticity in space. The computational cost is now of order $\mathcal{O}(nN)$, where n is the total number of eddies and N is the number of grid points. If the Biot-Savart kernel is evaluated directly, the cost is of order $\mathcal{O}(N^2)$.
- The use of the image vortices ensures that the wall normal component of the velocity at the wall is zero. The no-slip boundary condition, however, has to be separately enforced. We use a van Driest type damping function of the form $1 - e^{Az/\delta}$ for each component of the velocity field.
- The fluctuating thermodynamic fields are estimated using the Strong Reynolds Analogy (see, for instance, Smits and Dussauge¹⁸ for a discussion).

The computations mentioned above are inexpensive. Typically, for most of the inflow datasets used in this paper, the method took between 2 – 30 minutes on a desktop computer, depending on the size of the boxes. The results from a sample calculation are visualized using the imaginary part (‘swirl strength’) of the eigenvalues of the velocity gradient tensor are shown in figure (3). Four hierarchies were used. The eddy

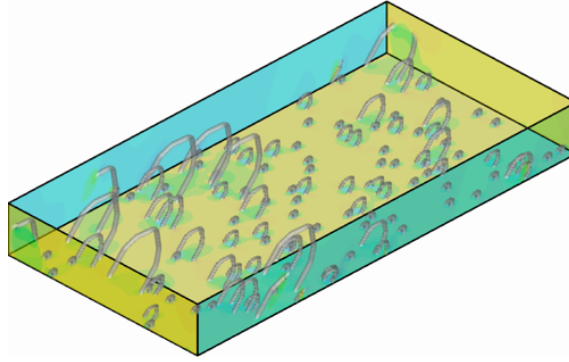


Figure 3. Hairpin vortices in a sample ‘eddy box’ visualized using the swirl strength computed from the velocity gradient tensor.

skeleton has four elements to it; the spanwise ‘bridge’ seen in fig. (2) is replaced with two straight segments forming a triangular arch. In this case, the damping function has not been applied.

The above procedure can be extended to include more sophisticated arrangements of eddies (‘packets’) or modified to account for more complicated geometries. Note that it would be impractical to resolve the scales in the inner layer since at moderate to high Reynolds numbers, it is comprised of extremely small-scale structures which are impossible to resolve on small/medium sized grids. The scheme is well suited, however, for LES or hybrid RANS/LES methods which do not resolve the wall.

II. *A priori* tests

Marusic and Perry⁷ compare the RMS values and Reynolds stresses predicted by the attached eddy hypothesis with data from turbulent boundary layers under a range of pressure gradients. Figure (4) shows a sample result from their paper. The symbols refer to experimental data for an adverse pressure gradient case at various Reynolds numbers and with varying values of the Coles’ wake factor (II). The reader is referred to the paper for details about the flow conditions. Marusic¹⁴ also computes the velocity auto-correlation and cross-correlation functions for the eddy shapes shown in figure (2). Figure (5) compares the autocorrelation of the streamwise component of the velocity for eddies arranged in the form of packets with experimental data from a flat plate turbulent boundary layer ($Re_\tau = 4700$, from Uddin¹⁵). The reader is referred to the paper by Marusic¹⁴ for further comparisons.

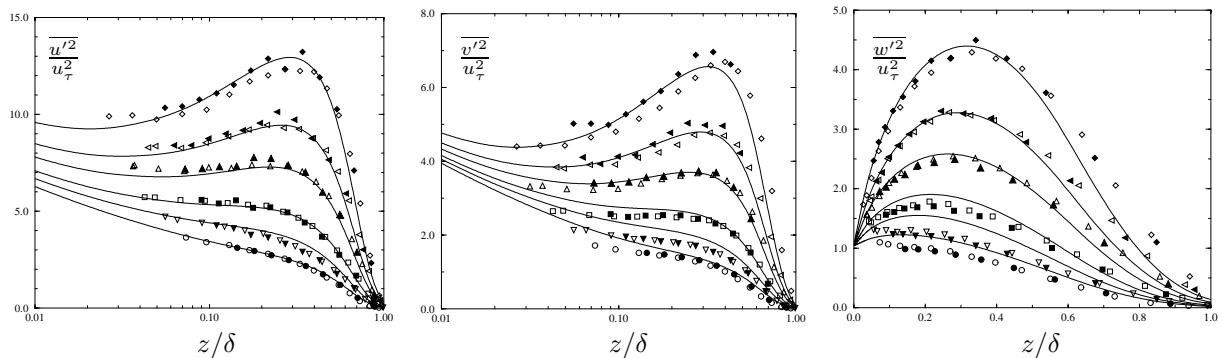


Figure 4. Reynolds normal stresses for an adverse pressure gradient flow case. Attached eddy formulation (lines) compared with experimental data (symbols). See Ref. (7) for an explanation of the symbols.

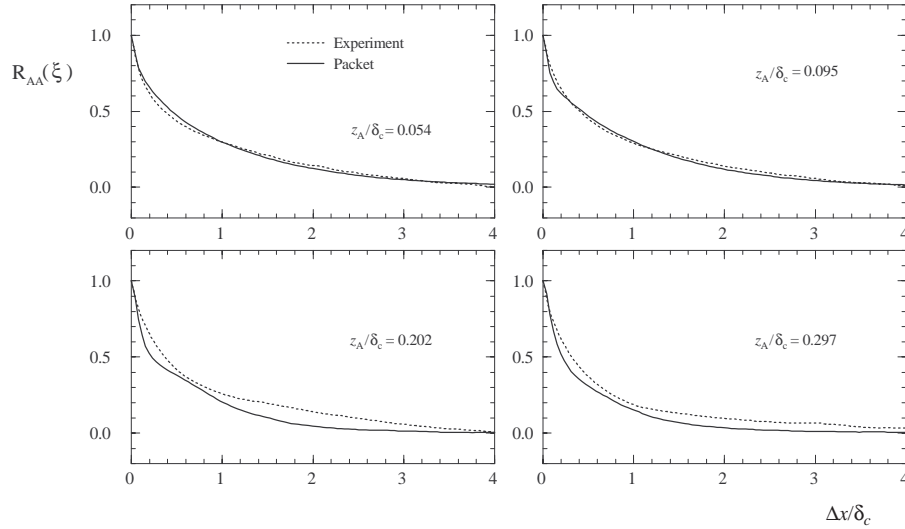


Figure 5. Autocorrelation results at different levels through the boundary layer. Solid line=attached calculation using eddies shown in figure (2a) arranged in packets, dotted lines=data from experiment.¹⁵

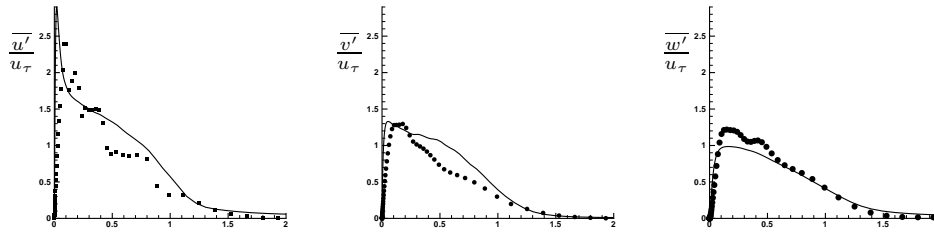


Figure 6. RMS values of velocity components computed from one precursor eddy box (symbols) compared to DNS data (lines) at similar conditions

The Reynolds stresses and autocorrelation function (and hence, the power spectrum) predicted by the model agrees well with experimental data. The above results were obtained analytically from the velocity field of one representative eddy by using the Fourier shift/scale theorems and Campbell's theorem (see Papoulis¹⁷) for uniform density shot-noise distributions.

In practice, however, one would use a set of pre-computed inflow data boxes. As an example, some statistics from one eddy box to be used in the computations are examined. The Mach number is 3 and the Karman number (Re_τ) is 4000. The streamwise spacing (Δx) (given by the time step used and the freestream velocity) is 0.05δ . The size of the precursor domain is set to be $6\delta \times 4\delta \times 6\delta$ in the x , y and z directions, respectively. The first point off the wall is less than 1 wall unit off the wall. Four hierarchies of eddies are used, with 8 eddies of the largest scale (δ), 16 of scale $\delta/2$ etc. The Biot-Savart calculation is done on a desktop and typically takes a few minutes to compute. The RMS values predicted by one such box compared to DNS data (Martin¹⁶) at a similar Mach number are shown in figure (6). The agreement, though not perfect, is reasonable, considering that no averaging is done over ensembles of data.

III. Numerical method

A finite-volume approach is used to solve the 3-D compressible Navier-Stokes equations with turbulence closure provided by the Spalart-Allmaras turbulence model²⁵ which has been modified to allow Detached Eddy Simulations (DES). The inviscid fluxes are computed using two different schemes: a low dissipation form of the Steger-Warming flux vector splitting method²⁶ with third-order upwind biased interpolation and a hybrid central/upwind scheme described below. The viscous fluxes and the turbulence source terms are evaluated using second-order accurate central differencing. The turbulence closure equation is fully coupled with the Navier-Stokes equations.

Implicit time integration is performed with the Full Matrix Data-Parallel method²⁷ which is fully parallelizable and allows large time steps to be taken to accelerate convergence. In a previous paper,³⁶ we discuss the effectiveness of the flux-evaluation method and some of the merits and demerits of the implicit time stepping scheme.

Two different solvers are used in the study: a structured, multi-block code and an unstructured solver (US3D).²⁸ The grids used in the unstructured solver are generated using the commercial packages GridPro and Gridgen. The viscous fluxes in the unstructured solver are evaluated using a weighted least-squares gradient approximation method.

We implement the DES method in the standard fashion²⁹ using the Spalart-Allmaras one-equation turbulence model with density corrections due to Catris and Aupoix³⁰ which is given as:

$$\frac{D\rho\tilde{\nu}}{Dt} = c_{b1}S\rho\tilde{\nu} - c_{w1}f_w\rho\left[\frac{\tilde{\nu}}{d_{DES}}\right]^2 + \frac{1}{\sigma}[\nabla \cdot (\mu\nabla\tilde{\nu})] + \frac{1}{\sigma}[\nabla \cdot (\sqrt{\rho\tilde{\nu}}\nabla(\sqrt{\rho\tilde{\nu}}))] + \frac{c_{b2}}{\sigma}(\nabla(\sqrt{\rho\tilde{\nu}}))^2.$$

The diffusion term in the standard Spalart-Allmaras model is replaced with a term that makes the model consistent with the logarithmic law for compressible boundary layers. This has an effect on the boundary layer profile and predictions of skin-friction in the attached boundary layer. The coefficients in the equation have the standard DES definitions: S is the magnitude of vorticity and d_{DES} is the DES length scale defined by $d_{DES} = \min(d, C_{DES}\Delta)$, where d is the distance to the closest wall, Δ is the largest dimension of the local cell and C_{DES} is an adjustable parameter which was calibrated by Shur *et al*³¹ in simulations of isotropic turbulence, and is 0.65.

Hybrid scheme

The paper by Ducros *et al*³² illustrates the de-aliasing property of the skew-symmetric form of the inviscid fluxes. We use the second and fourth order accurate (finite-volume form) fluxes constructed therein. The fluxes are non-dissipative. In this paper, shock capturing is done by adding the dissipative portion of the modified Steger-Warming scheme mentioned above. Consider the flux at a cell face denoted by $i + 1/2$ (cell centers are denoted by $i, i + 1$ etc.). The modified Steger-Warming flux is written as:

$$\begin{aligned} F_{i+1/2} &= (R\Lambda^+R^{-1})_{i+1/2}U_i + (R\Lambda^-R^{-1})_{i+1/2}U_{i+1} \\ &= (R\frac{\Lambda + |\Lambda|}{2}R^{-1})_{i+1/2}U_i + (R\frac{\Lambda - |\Lambda|}{2}R^{-1})_{i+1/2}U_{i+1} \\ &\approx \underbrace{\frac{1}{2}(F_i + F_{i+1})}_{\text{central}} - \underbrace{\frac{1}{2}(R|\Lambda|R^{-1})_{i+1/2}(U_{i+1} - U_i)}_{\text{dissipation}} \end{aligned}$$

In the equations above, U denotes the vector of conserved variables, R is the matrix of right-eigenvectors of the inviscid flux Jacobian $A(= \partial F/\partial U)$, and Λ is the diagonal matrix containing the eigenvalues of A . Higher order schemes are composed by replacing U_i and U_{i+1} by U_L and U_R , respectively, in the above equations, with U_L and U_R constructed at the face by upwind/upwind-biased interpolation.

In the hybrid scheme, the central portion of the flux is replaced by the skew-symmetric fluxes and dissipation is added selectively based on a sensor³³ ($\psi = \frac{(\nabla \cdot \bar{u})^2}{(\nabla \cdot \bar{u})^2 + (\nabla \times \bar{u})^2}$) which is able to distinguish between turbulent fluctuations and shocks. ψ takes on values very close to unity in regions where compression/dilatation is large and is small elsewhere. In practice, regions where ψ is larger than a small pre-assigned threshold value (typically ≈ 0.05) are marked as regions where the dissipation is actually applied. This way smooth regions of the flow are treating with the non-dissipative skew-symmetric fluxes and shocks are cleanly captured by the added dissipation. The scheme is similar to the one used by Pantano *et al.*³⁴ They use the skew-symmetric form of the fluxes in smooth regions of the flow and regions flagged using pressure and density curvature criteria are locally treated with a WENO scheme. Yee *et al.*³⁵ proposed a scheme where the dissipation is added in the form of a filtering step to the solution given by the non-dissipative operator. The scheme, though attractive, was found to be less stable at large CFL numbers compared to the case where the dissipation is applied prior to the time-advancement.

IV. Results

We consider two widely different flows: gaseous injection (of helium) into a supersonic crossflow (air), which is essentially a flat plate turbulent boundary layer; and a mixing layer formed by the merger of turbulent boundary layers separated by a thin splitter plate. For the injector flow, two cases, one with normal injection and the other with angled injection are discussed in this paper. A detailed discussion of the helium injection flows can be found in the paper by Peterson *et al.*²¹

It must be noted that in the injection simulations, the DES model is operating in a regime which it is not calibrated for. The switch between the RANS and the LES takes place within the boundary layer. Calculations performed using DES in this mode are usually found to be erroneous, in the sense that the top part of the mean velocity profile is found to be too ‘high’, the RMS values are incorrect and the skin friction is underpredicted. However, the inflow boundary for these cases is placed quite close to the injector, and the jet-crossflow interaction takes place before the mean properties of the boundary layer are corrupted. It is possible that the flow further downstream of the injection hole is affected by this.

The streamwise length of the eddy boxes used in the calculations was large compared to the boundary layer thickness (of the order of $30 - 70\delta$). This was done to avoid bias that would result from the use of a short eddy box in a time-periodic manner.

Gaseous injection into supersonic crossflow

Normal Injector

The first case that was simulated is discussed in the paper by Barber *et al.*²⁰ In this case, helium is injected normally through a circular injector. The freestream Mach number is 3, and the freestream total temperature and pressure are 294 K and 6.5 atm, respectively. The helium is injected with a total temperature of 299 K and a total pressure of 120 kPa, resulting in a mass flow rate of 0.89 g/s. The crossflow boundary layer thickness was found to be 4.1mm. The grid used for simulations of this case encompassed the first two data planes presented by Barber *et al.* and consists of 3.81 million cells. The DES simulations with the synthetic inflow boundary layer used an eddy box 73δ long.

Simulation of this case with the DES formulation without the synthetic inflow boundary layer results in a flow field absent of any large, unsteady motions as seen in figure (7). The introduction of the perturbations in the synthetic inflow boundary layer causes the flowfield to become greatly unsteady, and results in large undulations of the jet plume as seen in the instantaneous helium mass fraction contours of figure (7). The contours in the figure are distributed exponentially, and indicate vastly more mixing in the case with the synthetic inflow than in the case without.

Experimental measurements of time-averaged helium mass fraction were made at several downstream planes normal to the flow direction. Figure (8) shows the measurements, as well as the results from DES,

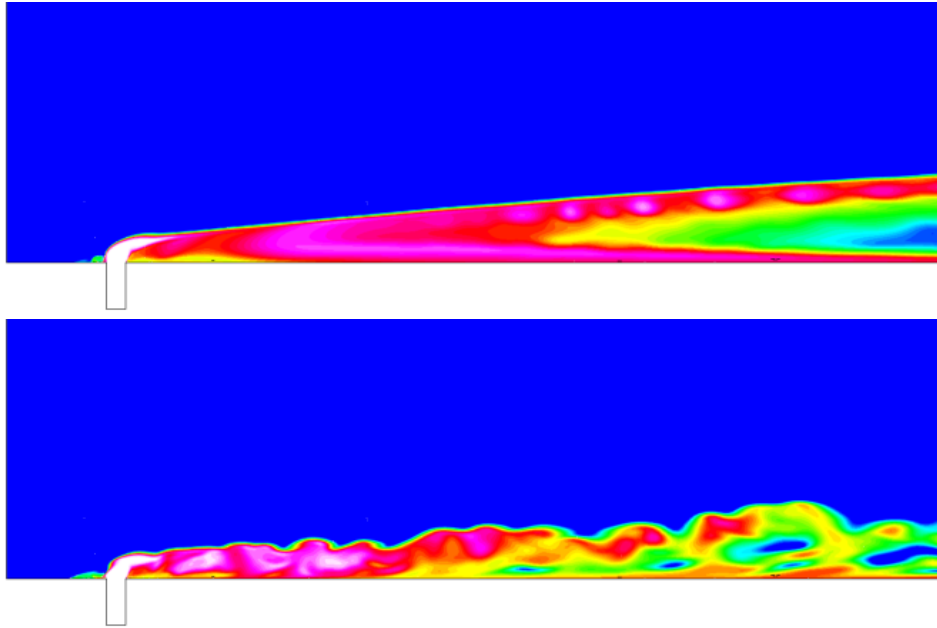


Figure 7. Instantaneous contours of helium mass fraction of normal injection for DES without eddies (top) and DES with eddies (Bottom). Contours are distributed exponentially.

with and without the synthetic inflow boundary layer, and RANS simulations for a plane 25.3 injector diameters downstream of the injector port. The results reiterate the enhanced mixing that results from the use of the synthetic inflow boundary layer. Without the eddies, the maximum mean helium concentration is predicted as 0.967, greatly exceeding the measured value of 0.12. With the eddies, DES gives a mean maximum concentration of 0.187. While still larger than the measured value, this is much more comparable to the experiment. The RANS also over-predicts the value, giving a maximum of 0.155. It is also seen that the presence of the unsteady boundary layer lowers the location of the jet core (defined as the region containing the maximum mean helium mass fraction) and increases the lateral mixing, resulting in a mean profile that is more in accordance with the experiment.

Figure (9) shows helium mass fraction contours 43.9 injector diameters (equivalent to 97 ‘effective diameters’, defined as³⁷ $R_b = \sqrt{\dot{m}_j / \rho_\infty u_\infty}$) downstream of the injector port. Without the unsteady boundary layer, the DES shows no discernable growth in the area of the jet plume, and the concentration gradients on the boundaries of the jet plume remain large. The maximum mean helium mass fraction is again several times larger than the measured value, 0.326 and 0.072, respectively. With the eddies, the jet plume is seen to grow in area, and the boundary of the plume is more representative of what is seen in the experiment. The maximum mean concentration is also more in line with the experiment, having a value of 0.079. While the wall normal coordinates of the jet core are higher for the DES with the synthetic boundary layer than in the experiment, the rate of penetration of the core is found to be comparable.²¹ Without the eddies the DES is found to over-predict the rate of core penetration. RANS is found to under-predict the penetration rate.

Angled Injector

The experimental configuration is discussed in the paper by Maddalena *et al.*²² It consists of a single injector angled at 30° with respect to the freestream. The freestream Mach number was 4, with total temperature and pressure of 295 K and 1034 kPa, respectively. The helium was heated to a total temperature

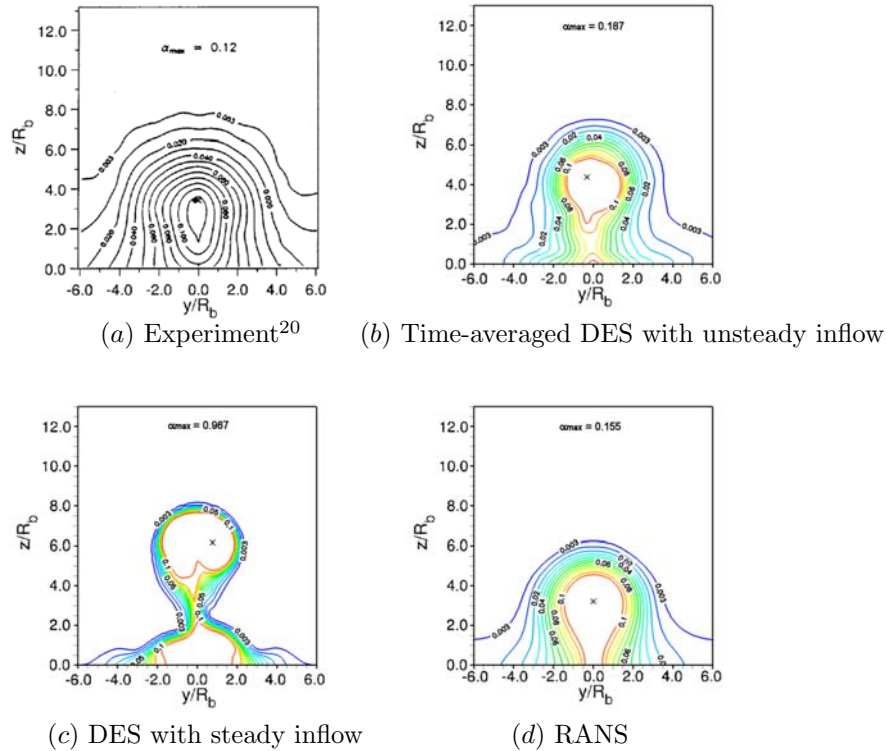


Figure 8. Helium mass fraction contours for normal injection case at plane $x/R_b = 56$ downstream of origin. Symbol \times marks location of maximum helium mass fraction. R_b is the effective diameter defined as³⁷ $R_b = \sqrt{\dot{m}_j / \rho_\infty u_\infty}$.

of 313 K and injected with a jet-to-freestream momentum flux ratio of 2.1. The helium mass flow rate is 3.4 g/s and the incoming boundary layer was estimated to be ≈ 13 mm thick. The grid used to simulate the case consists of 1.65 million cells. The eddy box used for the unsteady inflow case was 30δ long.

Shown in Fig. (10) are helium mass fraction contours from the experiment, DES with and without the unsteady inflow, and RANS simulations. The plane of data is 16.4 injector diameters downstream of the injector port. Comparing the DES with and without the eddies we see a large increase in the amount of mixing of injectant and freestream air. While the DES without the eddies gives a maximum helium mass fraction of 0.978, the DES with the eddies gives a maximum mean value of 0.354, which matches the experimentally measured value of 0.358 well. The presence of the eddies is also seen to increase the spanwise and wall normal direction mixing of the jet plume. Without the eddies the jet plume is found to be only 5.2 injector diameters wide (based on the lowest contour level), whereas with the eddies the jet plume is 6.9 diameters wide. The experiment also gives a width of 6.9 diameters.

The disagreement between the experiment and the DES with the unsteady inflow is in the core of the jet plume. The experiment has a kidney or horseshoe shaped core, whereas the DES shows two distinct cores that correspond to the centers of the counter-rotating vortex pair (CVP). The CVP is found to be excessively strong and the DES without the eddies shows a region of very little helium between the CVP cores. With the eddies, the CVP is weakened, on average, allowing for higher helium concentration between the CVP. However, even with the unsteady inflow, the CVP is still too strong, causing the formation of the two cores.

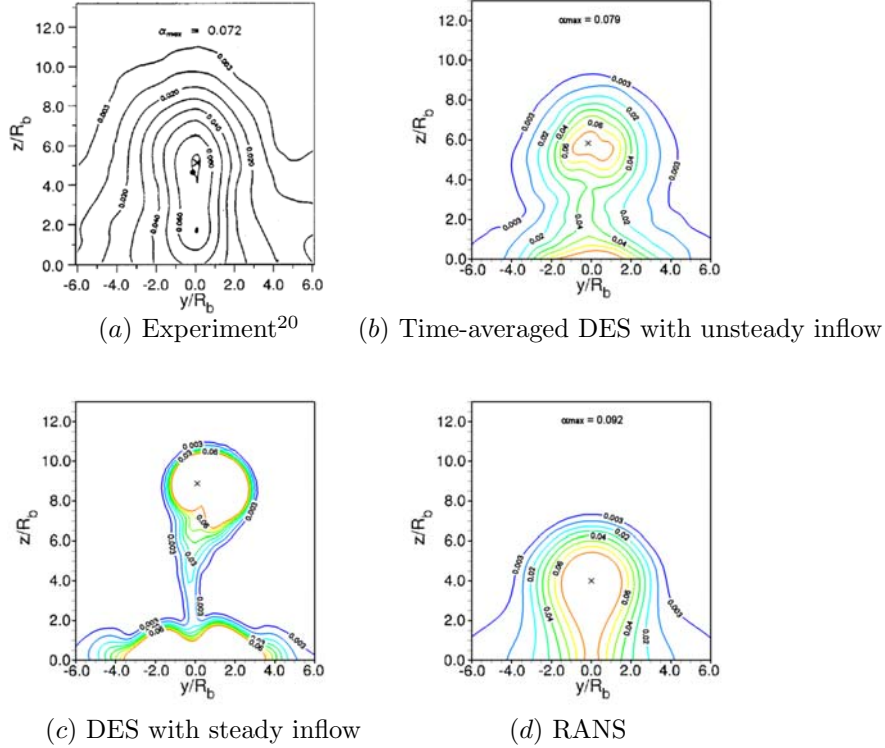


Figure 9. Helium mass fraction contours for normal injection case at plane $x/R_b = 97$ downstream of origin.

The turbulent fluctuations that are present in the flow make the flowfield generated by the DES with synthetic inflow more realistic than the RANS simulation. Comparing the instantaneous helium mass fraction contours of fig. (11) to the mean helium mass fraction of fig. (10b), it is clear that the DES predicts large local fluctuations and intermittency in the helium concentration. The RANS, as expected, predicts no fluctuations. While reproducing the correct mean values is no doubt important, producing meaningful instantaneous flow fields is of utmost importance for these flows.

Supersonic mixing layer

Experimental conditions

Goebel and Dutton³⁸ performed a series of benchmark experiments in which compressible turbulent mixing layers with a range of relative Mach numbers were examined. We simulate one of these cases (referred to as case 2 in their paper) with the aim of examining the effect of the unsteady inflow boundary condition. A schematic of the flow configuration is shown in figure 12. The subscripts 1 and 2 refer to conditions in the primary (top) and secondary (bottom) streams, respectively. The exit height of each stream (h) is 24mm and the width is 96mm in the experiment. The two streams were brought together at an angle of 2.5° across a thin splitter plate of thickness ≈ 0.5 mm. Laser Doppler velocimetry and schlieren imaging were used to examine the flowfields. For the case we are considering, the relevant parameters are shown in table (1).

In the table, T_t refers to total temperature, δ is the boundary layer thickness on the splitter plate, M_c is the convective Mach number, and $M_r = \Delta U/\bar{a}$ is the relative Mach number. The overbar corresponds to an

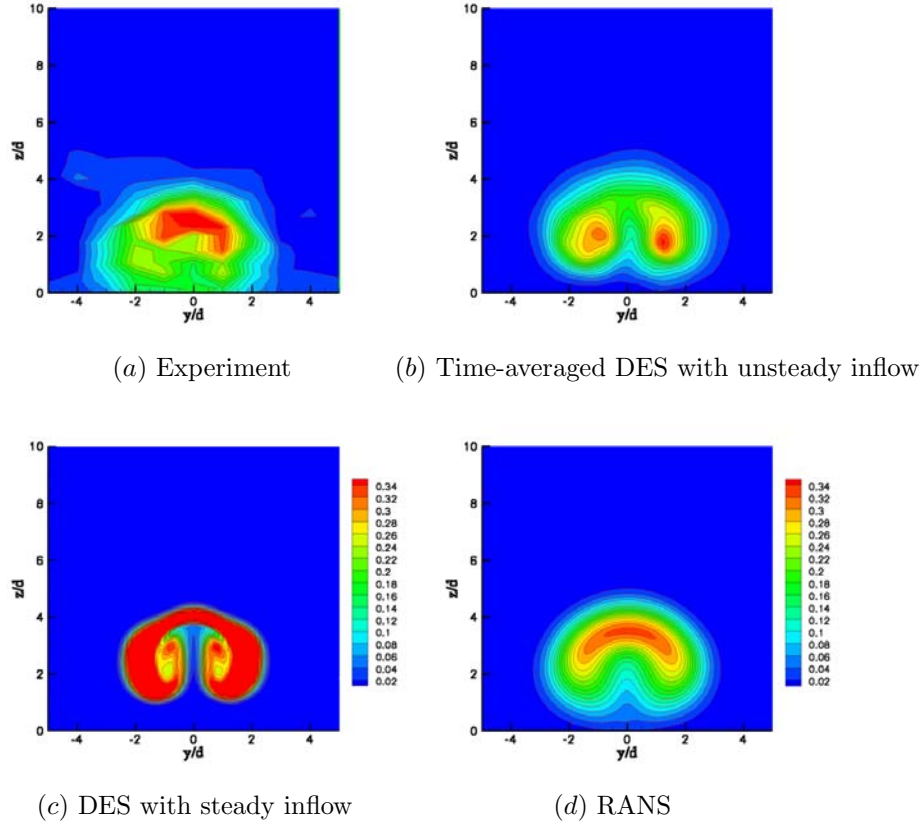


Figure 10. Helium mass fraction contours for Maddalena case at plane 16.4 d downstream of origin.

average of the top and bottom stream values.

Details of the computation

The computational domain extends from the tip of the splitter plate to a streamwise distance, $L_x = 300$ mm. The boundary layer profiles on the splitter plate were obtained using separate RANS calculations and the boundary layer thickness on each side (δ_1 , δ_2) was matched to the experimental value. The grid consisted of ≈ 1.8 million cells, with 600 points in the streamwise direction (x), 128 points in the transverse direction (z) and 24 points in the spanwise direction. The full height of the experimental domain (h) was considered. However, only a fraction of the spanwise length (13 mm) was simulated, owing to the large computational cost. Note that the spanwise length corresponds to $\approx 4.5\delta_1$, with a grid spacing of $0.18\delta_1$. The grid is

Stream	M	$U(ms^{-1})$	ρ	T_t	T	$\delta(mm)$	M_c	M_r	$Re = \bar{\rho}\Delta/\bar{\mu}$ ($10^6/m$)
Top	1.91	700	0.51	578	334	2.9	0.46	0.91	12
Bottom	1.36	399	0.79	295	215	2.5	"	"	"

Table 1. Flow parameters for the mixing layer

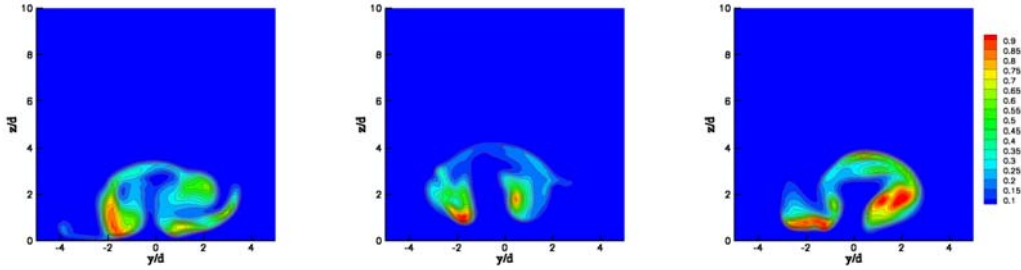


Figure 11. Instantaneous DES helium mass fraction contours for Maddalena case. Frames are $12.4\mu\text{s}$ apart, starting at left. Note the different scale than in Fig. (10)

constructed such that the incoming boundary layer is fully resolved (the first point off the wall is at $y^+ = 1$ and there are ≈ 30 points in the boundary layer on each side of the splitter plate). The grid points are packed towards the tip of the splitter plate in the streamwise direction as well, so as to capture the tip vortices. Consequently, the region near the splitter plate tip is very well resolved. Supersonic outflow conditions are imposed at the exit boundary (on the far right in the schematic (figure 12) and slip boundary conditions are imposed on the upper and lower surfaces of the domain. The wall of the splitter plate tip is treated as a viscous wall with no-slip boundary conditions. Periodic boundary conditions are used in the spanwise direction. The fluxes are computed using the low-dissipation hybrid scheme mentioned earlier in the paper. The time step used is $0.1\mu\text{s}$. This gives a CFL number of 25; larger time steps were found to be overly dissipative.

Steady inflow

First, we consider the case where the incoming boundary layer is steady. Figure (13a) shows instantaneous density contours in the x - z plane for this case. Compression and expansion waves originating from the tip of the splitter plate are clearly seen, along with a row of tip vortices that are shed periodically. The mixing layer is then seen to be relatively quiescent to a length of $\approx 170\text{mm}$, at which point turbulence seems to originate ‘spontaneously’. There is no evidence of organized large-scale structures as seen in subsonic mixing layers; this is in accord with experiment.

After the flow was deemed to have reached a statistically steady state, statistics were compiled over five flow times (based on L_x and U_2). Figure (14) compares mean and RMS values with experimental data for this case.

The mean velocity profiles are less developed than the corresponding experimental ones; the slopes of the velocity profile lag the measured values noticeably. Note also the undershoots in the velocity profiles at the first three stations. This seems to indicate the passage of organized vortex structures. Although the graph of u' (fig. 14b) at the $x = 300\text{mm}$ station seems to match the measured data well, the overall agreement is rather poor. The plots of u' and w' at the first two stations shown (at 100mm and 150mm from the tip) are narrower and lower in amplitude than they should be. The results indicate that the growth of the mixing layer is delayed compared to experiment. Georgiadis *et al*³⁹ also performed a hybrid RANS/LES simulation of the same flow case with steady inflow conditions. The mean value of the streamwise velocity was found to compare well with experiment. However, the RMS values were found to be consistently higher and the curves are broader than the corresponding experimental ones. The size of the domain in the spanwise direction was smaller (by a factor of 2) than the one used here. The role of the LES model (Smagorinsky with a range of values for the Smagorinsky ‘constant’ C_s , in their case, and DES in ours) may also have a large influence on the results.

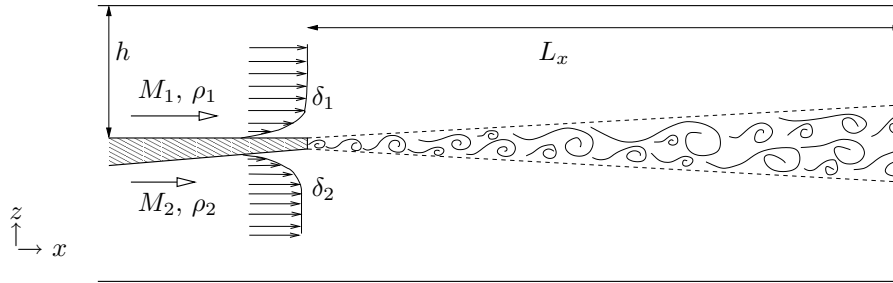


Figure 12. Schematic of the mixing layer configuration

Unsteady inflow

The boundary layer profiles at the inflow are modulated using our synthetic turbulence generation method. Owing to the relatively small time step, the box sizes used were restricted to 6δ (Taylor's hypothesis dictates the streamwise grid spacing in the box). Four hierarchies of eddy structure (ranging in size from δ to $\delta/8$) were used and the Strong Reynolds Analogy (also referred to as Morkovin's hypothesis) was used to compute the fluctuating density and temperature fields. The structures being fed in are comparable in scale to the tip vortices that are shed from the splitter plate. Presumably, there is a strong interaction between them. This is evident in figure (13b) which shows instantaneous density contours for this case. The difference is striking. The elongated row of tip vortices is broken up very close to the splitter plate and turbulence sets in almost immediately. The flow features, especially the thin, angled structures seem to resemble those commonly seen in schlieren images of compressible turbulent mixing layer flow-fields. Small scale features are also evident, indicating that the hybrid flux evaluation scheme is performing adequately.

The time averaged profile of streamwise velocity and RMS values of streamwise and transverse velocity are plotted in figure (15). The mean velocity (fig. (15a)) is in good agreement with experimental data. The slopes are correct, indicating that the growth rate is well matched. The plots of u' and w' , in figs. (15b, 15c) are also fairly accurate. Overall, there is a marked improvement in the quality of the results when the unsteady inflow is used.

Conclusions

A means of constructing synthetic turbulent boundary layers was explored. The method is extremely inexpensive, computationally. Additionally, values of Reynolds stress which are difficult to predict from experiment/RANS do not need be known *a priori*. Two different flows were examined for the effect of unsteady inflow fields generated using this new method. Normal and angled injection of helium into a crossflow was considered and highly unsteady motion of the jet plumes was observed. The effect of using the synthetic boundary layer was found to considerably improve predictions of mean helium concentration compared to using DES with steady inflow. Some unresolved issues such as the unusually high strength of the counter rotating vortex pair and the rate of separation of the jet plume from the wall need further exploration. However, given the difficulty of simulating jet interaction flows with supersonic crossflows, the results were found to be promising. A mixing layer formed by the interaction of two turbulent boundary layers was also simulated. The unsteady inflow has a positive influence on the spatial flow development. The results, overall are very encouraging and we feel that further investigations to characterize the method in other flows is merited.

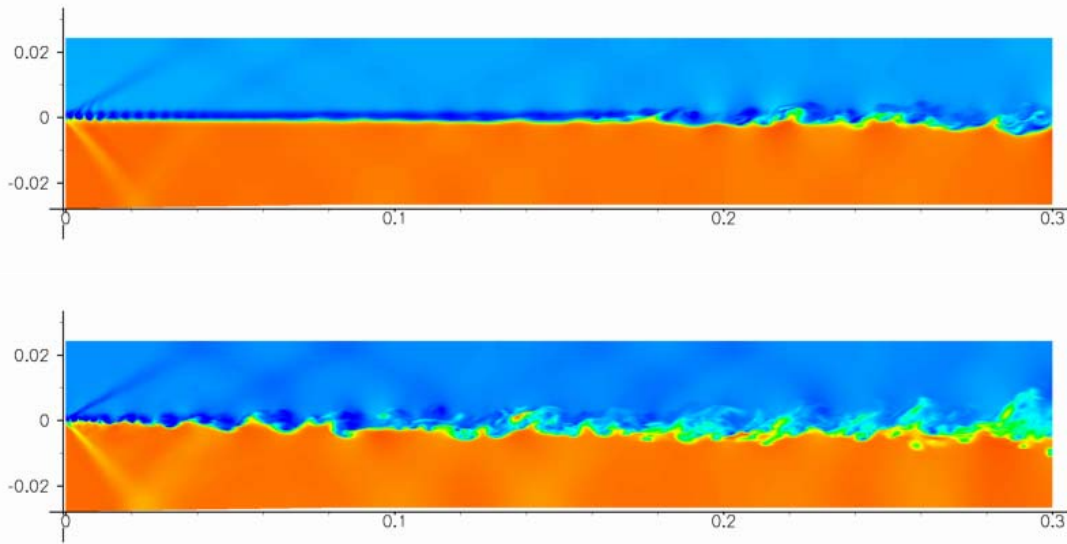


Figure 13. Instantaneous density contours: (a) steady inflow (b) unsteady inflow

Acknowledgments

The authors would like to thank Luca Maddalena, Theresa Campioli and Professor Joseph Schetz of Virginia Tech for data from their helium injection experiments. We also thank Professor Craig Dutton at the University of Texas at Arlington for the experimental data used in the mixing layer comparison and Professor Pino Martin at Princeton University for DNS data used in some of the comparisons. This research is supported by the Air Force Office of Scientific Research under grant Nos. FA9550-04-1-0341 and FA9550-04-1-0389. The views and conclusions contained herein are those of the authors and should not be interpreted as necessarily representing the official policies or endorsements, either expressed or implied, of the AFOSR or the U.S. Government.

References

- ¹Keating, A., Piomelli, U., Balaras, E. and Kaltenbach, H-J., “A *priori* and *a posteriori* tests of inflow conditions for large-eddy simulation”, *Physics of Fluids*, 16, 12, 2004.
- ²Townsend, A. A., *The Structure of Turbulent Shear Flow*, Cambridge University Press, Cambridge, 1956.
- ³Townsend, A. A., *The Structure of Turbulent Shear Flow*, Vol.2., Cambridge University Press, Cambridge, 1976.
- ⁴Perry, A. E. and Chong, M. S., “On the mechanism of wall turbulence”, *Journal of Fluid Mechanics*, Vol. 119, 1982.
- ⁵Perry, A. E., Henbest, S. M., and Chong, M. S., “A theoretical and experimental study of wall turbulence”, *Journal of Fluid Mechanics*, Vol. 165, 1986.
- ⁶Perry, A. E. and Marusic, I., “A wall-wake model for the turbulence structure of boundary layers. Part 1. Extension of the attached eddy hypothesis”, *Journal of Fluid Mechanics*, Vol. 298, 1995.
- ⁷Marusic, I. and Perry, A. E., “A wall-wake model for the turbulence structure of boundary layers. Part 2. Further experimental support”, *Journal of Fluid Mechanics*, Vol. 298, 1995.
- ⁸Adrian, R. J., Meinhart, C. D. and Tomkins, C. D., “Vortex organization in the outer region of the turbulent boundary layer”, *Journal of Fluid Mechanics*, Vol. 422, 1, 2000.
- ⁹Meinhart, C. D., and Adrian, R. J., “On the existence of uniform momentum zones in a turbulent boundary layer”, *Physics of Fluids*, 7, 1995.
- ¹⁰Kim, K. C., and Adrian, R. J., “Very large-scale motions in the outer layer”, *Physics of Fluids*, 11, 1999.

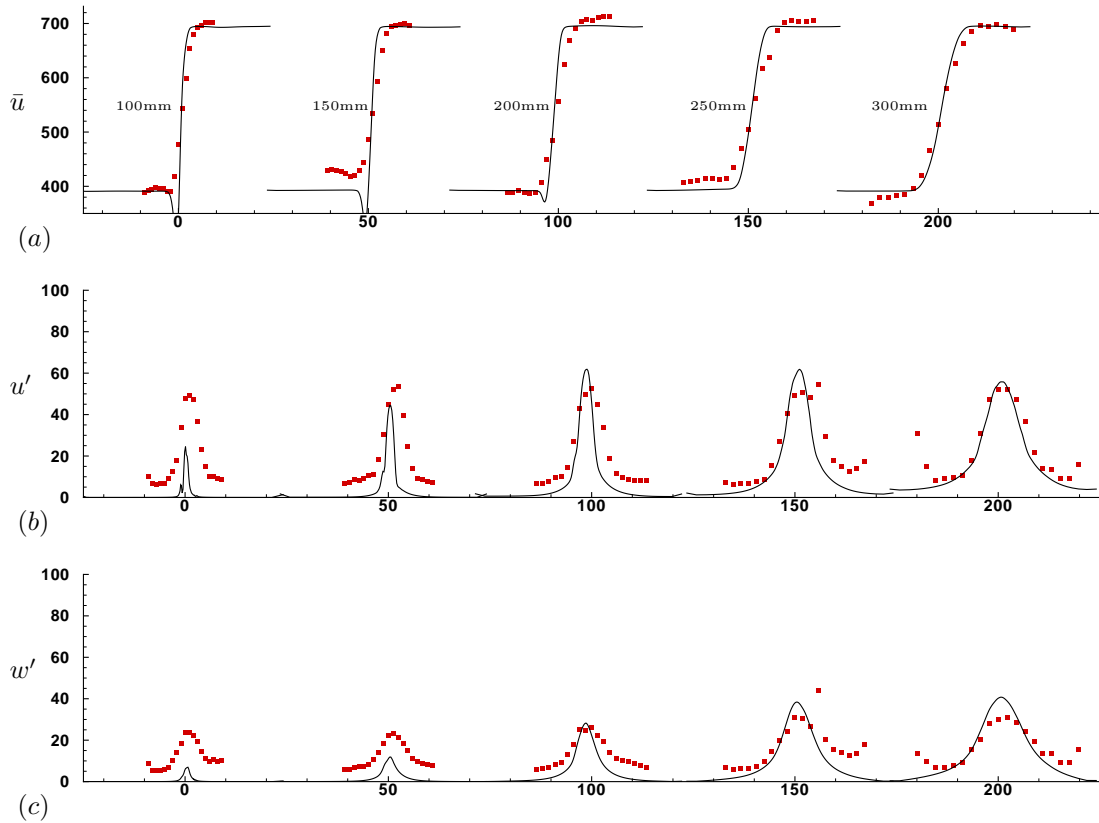


Figure 14. Steady inflow : time averaged values of (a) streamwise velocity, (b) RMS values of streamwise velocity fluctuations and (c) RMS values of transverse velocity fluctuations. The streamwise offsets from the splitter plate tip of the station at which the profiles are compared are shown in figure (a). Symbols=Experiment,³⁸ lines=computation

¹¹Zhou, J., Adrian, R. J., Balachander, S. and Kendall, T. M., “Mechanisms for generating coherent packets of hairpin vortices in channel flow”, *Journal of Fluid Mechanics*, Vol. 387, 1999.

¹²Zhou, J., Adrian, R. J. and Balachander, S., “Autogeneration of near wall vortical structure in channel flow”, *Physics of Fluids*, 8, 1996.

¹³Liu, Z. C. and Adrian, R. J., “ Evidence for hairpin structure in DNS of channel flow”, *Proceedings: Turbulence and Shear Flow Phenomena 1*, Santa Barbara, CA, 1999.

¹⁴Marusic, I., “On the role of large-scale structures in wall turbulence”, *Physics of Fluids*, 13, 3, 2001.

¹⁵Uddin, A. K. M., “The structure of a turbulent boundary layer”, Ph.D Thesis, University of Melbourne, Australia, 1994.

¹⁶Martin, P. M., *Private communication*

¹⁷A. Papoulis, “Probability, Random Variables and Stochastic Processes” (McGraw-Hill, New York, 1965)

¹⁸Alexander J. Smits and Jean-Paul Dussauge, “Turbulent Shear Layers in Supersonic Flow” (Springer Science+Business Media Inc., 2006)

¹⁹McCann, G .J. and Bowersox, R. D. W., “Experimental investigation of supersonic gaseous injection into a supersonic freestream”, *AIAA Journal*, Vol. 34, No. 2, February 1996.

²⁰Barber, M.J., Schetz, J.A., Roe, L.A., “Normal, Sonic Helium Injection Through a Wedge- Shaped Orifice into Supersonic Flow,” *Journal of Propulsion and Power*, Vol. 13 No. 2, March-April 1997.

²¹Peterson, D.M., Subbareddy, P.K., Candler, G. V., “Simulation of Injection Into a Supersonic Crossflow Using DES with Synthetic Inflow,” AIAA paper 2006-3326.

²²Maddalena, L., T. L. Campioli, and J. A. Schetz, “Experimental and Computational Investigation of an Aeroramp

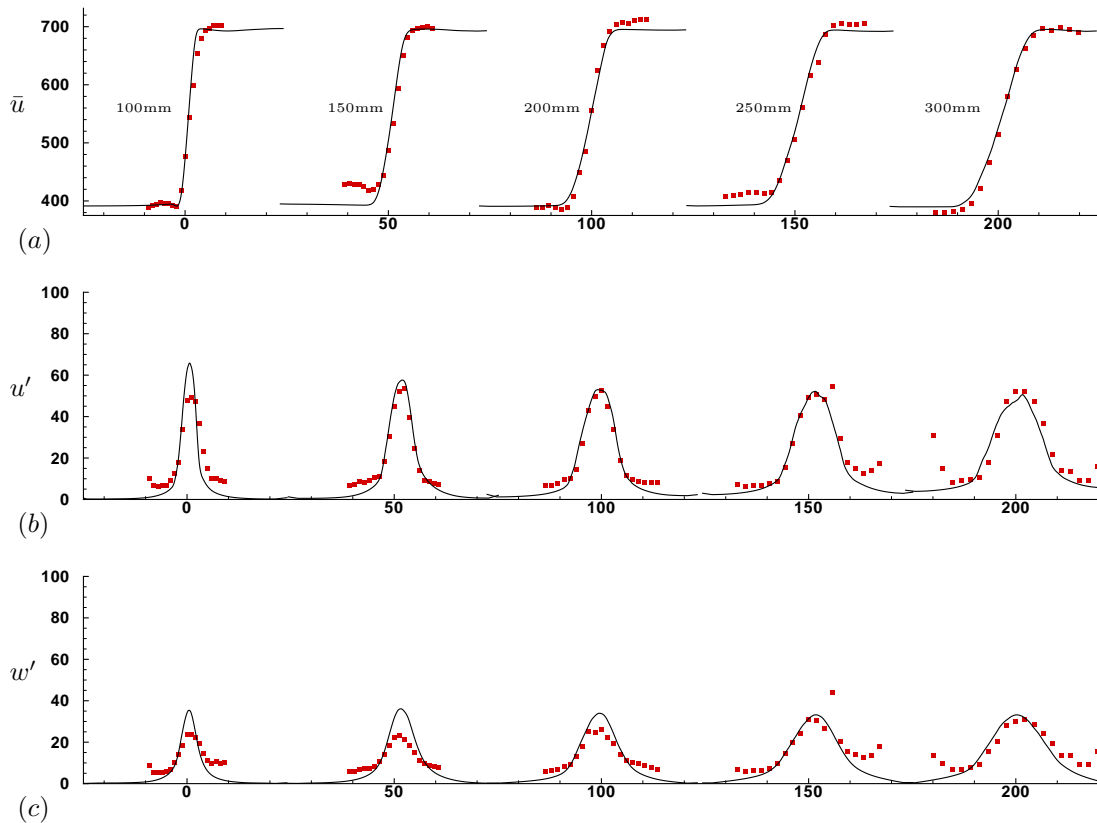


Figure 15. As in figure (14), but with unsteady inflow.

Injector in a Mach Four Cross Flow,” AIAA/CIRA 13th International Space Planes and Hypersonics Systems and Technologies Conference, Capua, Italy, May 16-20, 2005.

²³Martin, M. P., and Candler, G. V., “DNS of a Mach 4 boundary layer with chemical reactions”, *AIAA 2000-0399*, 2000.

²⁴Subbareddy, P. and Candler G. V., “Numerical investigations of supersonic base flows using DES”, *AIAA 2005-0886*, 2005.

²⁵Spalart P.R., Allmaras S.R., “A one equation turbulence model for aerodynamic flows,” *AIAA Paper 1992-0439*, 1992.

²⁶MacCormack, R.W. and Candler, G.V., “The Solution of the Navier-Stokes Equations Using Gauss-Seidel Line Relaxation,” *Computers and Fluids*, Vol. 17, No. 1, pp. 135-150, 1989.

²⁷Wright, M.J., Candler, G.V., and Prampolini, M., “Data Parallel Lower-Upper Relaxation Method for the Navier-Stokes Equations,” *AIAA Journal*, Vol. 34, No. 7, pp. 1371-1377, July 1996.

²⁸Nompelis, I., Drayna, T. W. and Candler, G.V., “Development of a Hybrid unstructured implicit solver for the simulation of reacting flows over complex geometries” *AIAA Paper 2004-2227*, June 2004.

²⁹Strelets, M., “Detached Eddy Simulation of Massively Separated Flows”, *AIAA Paper 2001-0879*, 2001.

³⁰Stephane Catris and Bernard Auipoix, “Density corrections for turbulence models,” *Aerosp. Sci. Technol.*, 4, 2001.

³¹Shur, M., Spalart, P. R., Strelets, M., and Travin, A., “Detached Eddy Simulation of an Airfoil at High Angle of Attack”, 4th Int. Symp. Eng. Turb. Modeling and Measurements, Corsica, May 24-26, 1999.

³²Ducros, F., Laporte, F., Soulères, T., Guinot, V., Moinat, P. and Caruelle, B., “High-order fluxes for conservative skew-symmetric like schemes in structured meshes: Application to compressible flows”, *Journal of Computational Physics* Vol. 161, pp. 114-139, 2000.

³³Ducros, F., Ferrand, V., Nicoud, F., Weber, C., Darracq, D., Gacherieu, C. and Poinso, T., “Large-eddy simulation of shock/turbulence interaction”, *Journal of Computational Physics* Vol. 152, pp. 517-549, 1999.

³⁴Pantano, C., Deiterding, R., Hill, D. J. and Pullin, D. I., “A low-numerical dissipation patahc based adaptive mesh refinement method for large-eddy simulation of compressible flows”, *Journal of Computational Physics*, (paper in submission)

³⁵Yee, H. C., Sandham, N. D. and Djomehri, M. J., “Low-dissipative high-order shock-capturing methods using characteristic-based filters”, *Journal of Computational Physics* Vol. 150, pp. 199-238, 1999.

³⁶Subbareddy, P. and Candler G. V., “Detached Eddy Simulation of Supersonic Base Flow with Bleed”, *AIAA 2004-0 066*, 2004.

³⁷Schetz, J.A., “Interaction Shock Shape for Transverse Injection in Supersonic Flow,” *Journal of Spacecraft and Rockets*, Vol. 7, No. 2, 1970, pp. 143-148.

³⁸Goebel, S. G. and Dutton, J. C., “Experimental study of compressible turbulent mixing layers” , *AIAA Journal*, Vol. 29, No. 4, April 1991.

³⁹Georgiadis, N. J., Alexander, J. I. D. and Reshotko, E., “Hybrid Reynolds-averaged Navier-Stokes/Large-eddy simulations of supersonic turbulent mixing” , *AIAA Journal*, Vol. 41, No. 2, February 2003.

⁴⁰Piomelli, U., Balaras, E., Pasinato, H., Squires, K. D. and Spalart. P. R., “The inner-outer layer interface in large eddy simulations with wall models ” , *International Journal of Heat and Fluid Flow*, Vol. 24, 2003.